

OPEN

Sea Surface Height Estimation with Multi-GNSS and Wavelet De-noising

Fade Chen¹, Lilong Liu^{2,3} & Fei Guo^{1*}

This paper presents a new sea surface height (SSH) estimation using GNSS reflectometry (GNSS-R). It is a cost-effective remote sensing technique and owns long-term stability besides high temporal and spatial resolution. Initial *in-situ* SSH estimates are first produced by using the SNR data of BDS (L1, L5, L7), GPS (L1, L2, L5), and GLONASS (L1, L2), of MAYG station, which is located in Mayotte, France near the Indian Ocean. The results of observation data over a period of seven days showed that the root mean square error (RMSE) of SSH estimation is about 32 cm and the correlation coefficient is about 0.83. The tidal waveform is reconstructed based on the initial SSH estimates by utilizing the wavelet de-noising technique. By comparing the tide gauge measurements with the reconstructed tidal waveform at SSH estimation instants, the SSH estimation errors can be obtained. The results demonstrate that the correlation coefficient and RMSE of the wavelet de-noising based SSH estimation is 0.95 and 19 cm, respectively. Compared with the initial estimation results, the correlation coefficient is improved by about 14.5%, while the RMSE is reduced by 40.6%.

Obtaining accurate Sea Surface Height (SSH) is significant for human living, especially for those live along ocean coasts. Furthermore, it is also important to coastal ecosystems and coastal morphology^{1,2}. SSH has been obtained primarily with tide gauges during the last centuries. While for the last three decades, satellite altimetry has been the dominating technique³⁻⁵. The satellite altimetry has unique advantages in monitoring sea surface topography in open ocean research such as ocean circulation⁶. However, due to tidal aliasing effect, its spatial and temporal resolution are insufficient to observe complex and rapidly changing dynamics which makes it difficult to use near the coast⁷. Meanwhile, tide gauges are affected by both sea level and land surface changes since the measurements are related to a benchmark on the land, where they were established. For these reasons, it is difficult to use traditional tide gauges for sea-level studies in tectonically active areas or applications related to changes in the global ocean volume, e.g., the global sea level budget⁸. These applications need absolute observations of sea level, in other words, measurements with respect to a terrestrial reference frame⁹.

In recent years, the reflected signals of Global Navigation Satellite System (GNSS) are used to retrieve a range of geophysical parameters such as SSH, soil moisture, ocean wind speed, etc.¹⁰⁻¹⁸. This technique is also termed GNSS-Reflectometry (GNSS-R), which exploits conventional receivers or low-cost, low-mass, and low-power characteristics of GNSS-R receivers. Different GNSS-R based methods have been proposed in the literature to measure a range of geophysical parameters. Basically, either a single antenna or two separate antennas are used for the direct and reflected signal reception. A number of researchers have investigated GNSS-based ocean surface altimetry by using the measurement of signal arrival time obtained by either mounting the receiver on an aircraft or fixing it on the ground such as on a bridge^{19,20}. Anderson *et al.* first proposed to use the interference pattern in the recorded Signal-to-Noise Ratio (SNR) to estimate SSH²¹. Later, Larson *et al.* applied the SNR method to SSH of the nearby ocean during three months²². Santamaría-Gómez *et al.* developed an approach to extract SNR data dominated by sea-surface reflections and to remove SNR frequency changes caused by the dynamic sea surface²³. They successfully demonstrated its ability to estimate local SSH and improved accuracy. Nevertheless, many of their studies used single frequency or single system. With constantly developing and perfecting of other navigation satellite systems such as Galileo and BDS, can we improve the accuracy of SSH estimation using multi frequencies or multi-systems? There are still many challenging problems to be resolved²⁴.

¹School of Geodesy and Geomatics, Wuhan University, Wuhan, 430079, China. ²College of Geomatic Engineering and Geoinformatics, Guilin University of Technology, Guilin, 541004, China. ³Guangxi Key Laboratory of Spatial Information and Geomatics, Guilin, 541004, China. *email: fguo@sgg.whu.edu.cn

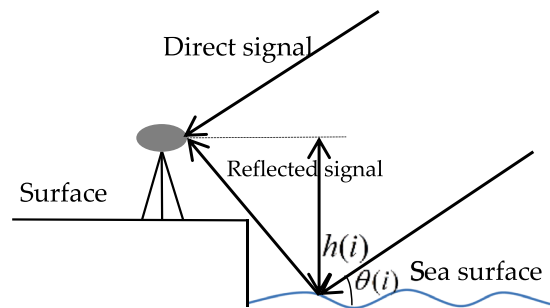


Figure 1. Diagram of GNSS-R for SSH variation.

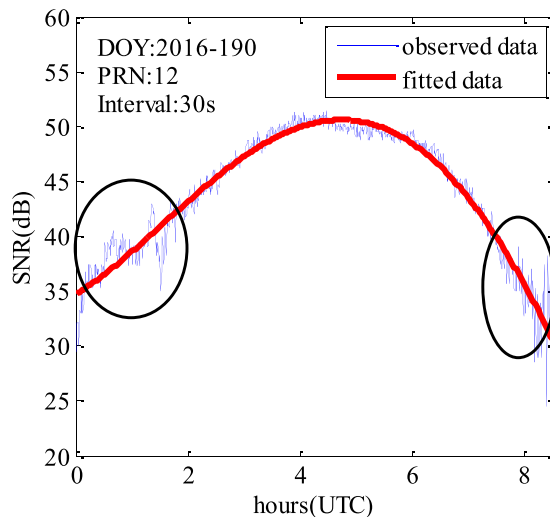


Figure 2. SNR variations observed by a BDS receiver.

In this paper, we propose an improvement of the method based on the SNR analysis of a single antenna. And the focus is on GNSS-R ocean surface altimetry based on the SNR data of multiple satellite constellations and multiple frequencies, namely BDS (L1, L5, L7), GPS (L1, L2, L5) and GLONASS (L1, L2). The purpose is to exploit measurements diversity to achieve a performance gain. The structure of the next part of this paper is organized as follows. Firstly, the fundamental theory of SSH GNSS-R and contains a wavelet analysis in detail are given. Thereafter the data introduction is presented. Then SSH estimation results by using individual GNSS-R and multi-GNSS-R are firstly shown. The SNR data collected by an IGS station are used for evaluation and analysis. Tide gauge observations are used as ground-truth data for performance comparison. Furthermore, the initial discrete SSH estimation results are used to reconstruct the tidal waveform by using wavelet de-noising technique. Finally, the concluding remarks are declared.

Theory and Methods

Methods of GNSS-R. Multipath propagation is one of the main GNSS error sources, which constrains high-precision positioning. The multipath caused by the difference of the phase between the direct and reflected signals will affect GNSS observations and give rise to oscillations in the observations. As a result, the SNR data recorded by a GNSS receiver with a single antenna will contain information about the interference, antenna height and hence SSH variation. Figure 1 shows the diagram of SSH estimation based on the SNR method. Here $h(i)$ is the antenna height relative to reflection surface, and $\theta(i)$ is the angle between the direct signal and the instantaneous sea surface of a specific scattering point. In Fig. 1, the reflected signal has one excess phase delay when compared to the direct signal, which is related to the antenna height $h(i)$.

Figure 2 shows an example of the SNR variations recorded by a BDS receiver. The thin blue fast-varying curve is the observed data, while the red thick smooth curve is the fitted SNR of the direct signal. As we can see, the multipath SNR is proportional to the difference between the observed curve and the fitted curve. It can be seen that the multipath SNR during the rising and setting of the satellite is significantly higher than that elsewhere, as shown in the two black ellipses.

SNR is one of the main observables of the GNSS receiver, which is mainly related to the satellite signal transmission power, antenna gain, and multipath effect. As the elevation angle increases, the antenna gain raises, subsequently, the direct signal SNR increases. In this paper, we use the observed SNR data from the GNSS receiver to estimate SSH. As described in²², the SNR is given by

$$\begin{aligned} \text{SNR} &= \frac{A^2}{2P_n} \\ &= \frac{1}{2P_n}(A_d^2 + A_r^2 + 2A_dA_r \cos\delta\phi(t)) \end{aligned} \quad (1)$$

where P_n is the noise power, A_d indicates amplitude of direct signal, A_r refers amplitude of the reflected signal, $\delta\phi(t)$ is the reflection excess phase with respect to direct phase (also known as the interferometric phase), given by

$$\delta\phi(t) = \frac{4\pi h}{\lambda} \sin\theta(t) \quad (2)$$

where h stands for antenna height from the specular scattering point on the reflected surface, λ is the carrier wavelength, $\theta(t)$ represents the elevation angle. Since (i) GNSS antennas are designed to filter reflected signals, (ii) the reflected signal is attenuated upon reflection, and (iii) the azimuth angles we choose to make reflected signals come from the sea surface, we can assume that

$$A_d \gg A_r \quad (3)$$

Therefore, the direct signal determines the overall trend of the SNR observations (see Fig. 2). So, we can use a low-order polynomial to fit the observed SNR data and then remove the trend. As a result, a detrended SNR time series is produced, which can be used to estimate the surface parameters such as SSH. As described in²², after removing the SNR trend, the remaining SNR can be approximated as

$$d\text{SNR} = A \cos\left(\frac{4\pi h}{\lambda} \sin\theta(t) + \varphi\right) \quad (4)$$

where φ indicates a phase offset, A denotes the amplitude which is given by

$$A = \frac{A_d \cdot A_r}{P_n} \quad (5)$$

By defining $\omega = \sin\theta$ and $f = 2h/\lambda$, Eq. (4) can be rewritten as

$$d\text{SNR} = A \cos(2\pi f\omega + \varphi) \quad (6)$$

Due to the tidal effect, the antenna height relative to the surface may change smoothly by around 0.72 m during half an hour at the selected observation station. Thus, the frequency of the detrended SNR signal varies gently with time. However, the mean frequency of the signal would be dominant, which basically corresponds to the antenna height at the middle of the observation time period.

From Eq. (6) and the definition of f , the antenna height is associated with the frequency of the detrended SNR signal by

$$h = f\lambda/2 \quad (7)$$

Spectral analysis is applied to obtain the spectral peak frequency of the time series. In this paper, the Lomb-Scargle periodogram (LSP) method is used since it can handle unevenly spaced samples²². The recorded SNR data are typically evenly sampled in time, but the sine of elevation angle is not evenly distributed. The LSP is a well-known algorithm for detecting and characterizing periodicity in unevenly-sampled time-series, even more, has seen particularly wide use within the astronomy community²⁵. As described in²⁵, the LSP method calculates the power spectral density by

$$P_x(f) = \frac{1}{2\delta^2} \left\{ \frac{[\sum(X_i - \bar{X})\cos\omega(t_i - \tau)]^2}{\sum\cos^2\omega(t_i - \tau)} + \frac{[\sum(X_i - \bar{X})\sin\omega(t_i - \tau)]^2}{\sum\sin^2\omega(t_i - \tau)} \right\} \quad (8)$$

where \bar{X} and δ^2 are the mean and the variance of the observed sequence respectively, ω denotes the angular frequency, and τ symbolizes the phase which can be inferred by

$$\tan(2\omega\tau) = \frac{\sum\sin(2\omega t_i)}{\sum\cos(2\omega t_i)} \quad (9)$$

As an example of obtaining the peak frequency using LSP method, Fig. 3 shows the results of LSP analysis of the detrended SNR time series from the SNR data observed by BDS satellite PRN09 on two different days. The elevation angles change from 5° to 20° and from 20° to 5° for day of year (DOY) 191 and DOY 193, respectively. The peak spectral frequency can be clearly observed. The peak frequency difference is caused by the variation in the SSH over the two various observation periods. The estimated peak frequency, besides, Eq. (7) are applied to obtain the antenna height.

Wavelet De-noising. The concept of wavelet was first proposed by Morlet in 1984²⁶. Later, under the help of Grossmann, Morlet formalized the continuous wavelet transform (CWT)²⁷ as follow

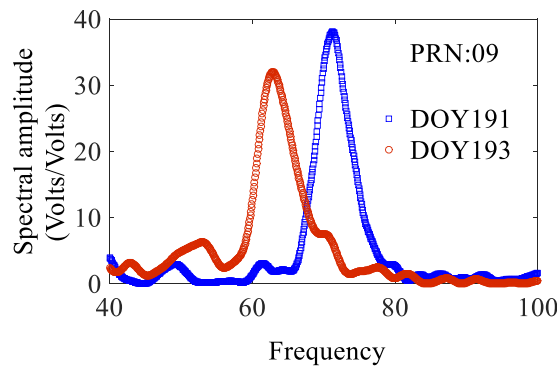


Figure 3. Detrended SNR spectrum produced by Lomb-Scargle periodogram analysis.

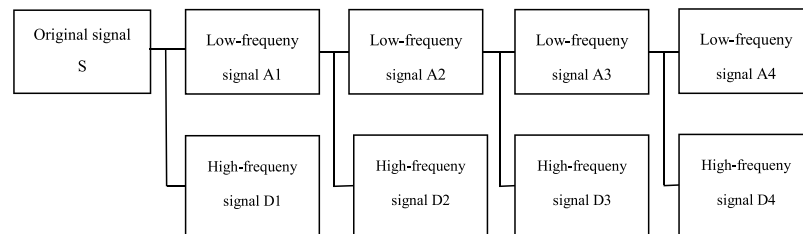


Figure 4. Wavelet decomposition filter model.

$$W_{\psi}f(a, b) = \langle f, \psi_{a,b} \rangle = a^{-1/2} \int_{-\infty}^{+\infty} f(t) \overline{\psi\left(\frac{t-b}{a}\right)} dt \tag{10}$$

where a indicates the scale parameter, b refers to the time parameter, $\psi(t)$ is an analyzing wavelet, and $\overline{\psi(\bullet)}$ symbolizes the complex conjugate of $\psi(\bullet)$. The inverse transform of CWT is given by

$$f(t) = \frac{1}{C_{\psi}} \int_{-\infty}^{+\infty} \left\{ W_{\psi}f(a, b) \left[a^{-1/2} \psi\left(\frac{t-b}{a}\right) \right] \right\} \frac{da}{a^2} \tag{11}$$

where a, b and t are continuous. However, they must be discretized in analyzing real data. The discrete method is called discrete wavelet transform (DWT). In practice, the scale a and the time b are discretized as following

$$a = a_0^j, \quad b = ka_0^j b_0 \tag{12}$$

where j and k are integers. And the continuous wavelet function $W_{\psi}f(a, b)$ become the DWT, given by

$$C_{j,k} = \int_{-\infty}^{+\infty} f(t) \overline{\psi_{j,k}(t)} dt \quad \text{with} \quad \psi_{j,k}(t) = 2^{-j/2} \psi(2^{-j}t - k) \tag{13}$$

The inverse transform of DWT is computed by

$$f(t) = \sum_{j \in \mathbb{Z}} \sum_{k \in \mathbb{Z}} C_{j,k} \psi_{j,k}(t) \tag{14}$$

Mallat proposed a fast DWT algorithm in 1989²⁸, which decompose and reconstruct the signal using the wavelet filters. The decomposition algorithm is given by

$$\left. \begin{aligned} A_j[f(t)] &= \sum_k H(2t - k) A_{j-1}[f(t)] \\ D_j[f(t)] &= \sum_k G(2t - k) A_{j-1}[f(t)] \end{aligned} \right\} \tag{15}$$

where $t = 1, 2, \dots, N$ is the discrete time serial number, N denotes the signal length, $f(t)$ symbolizes the original signal, $j = 1, 2, \dots, J$ is the decomposition level, J is the maximum decomposition level; H and G are the wavelet low-frequency and high-frequency pass decomposition filters, respectively; A_j and D_j are the wavelet coefficients of $f(t)$ in the low-frequency and the high-frequency part of the J th layer, respectively. Figure 4 shows the wavelet decomposition filter model.

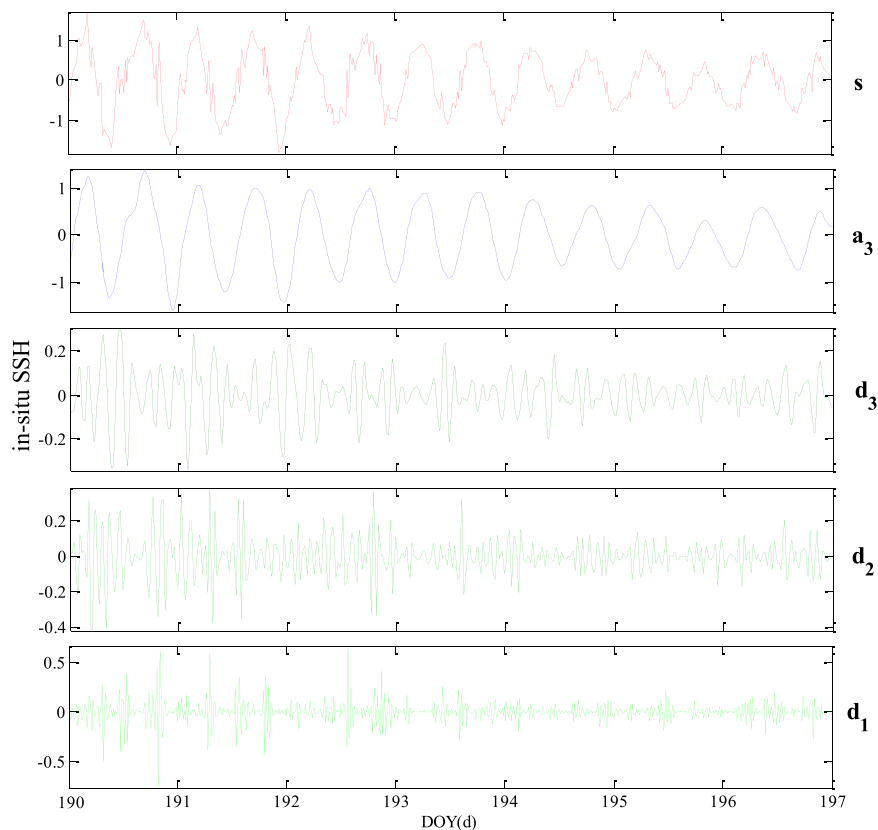


Figure 5. Results of wavelet decomposition of Db6 wavelet under 3rd level.

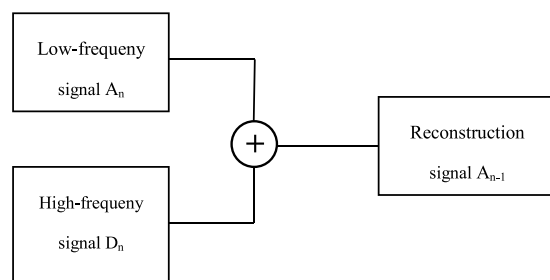


Figure 6. Wavelet reconstruction filter model.

Each signal has the following relationship: $S = A_1 + D_1$; $A_1 = A_2 + D_2$; $A_2 = A_3 + D_3$; $A_3 = A_4 + D_4$. As an example of decomposition, Fig. 5 shows the results of wavelet decomposition under Db6 wavelet with decomposition level 3, and the original signal S is the *in-situ* SSH estimation of this paper. In addition, the relationship of each signal is: $S = a_3 + d_3 + d_2 + d_1$, $a_3 = d_3 + d_2 + d_1$.

The reconstruction is given by

$$A_j[f(t)] = \sum_k h(2t - k)A_{j+1}[f(t)] + \sum_k g(2t - k)D_{j+1}[f(t)] \tag{16}$$

where h and g represents the wavelet low pass and high pass reconstruction filter, respectively. Other symbols are the same as Eq. (15). Figure 6 shows the wavelet reconstruction filter model.

One important step of wavelet de-noising is choosing the appropriate wavelet function $W_{ij}(a, b)$. Wavelet functions such as Daubechies (dbN), Haar, and Symlets (SymN) are commonly used for wavelet analysis. To choose a suitable wavelet function, the performance of db6, Haar and Sym2 at different levels are analyzed in section “Improved SSH estimates with Wavelet De-noising”.

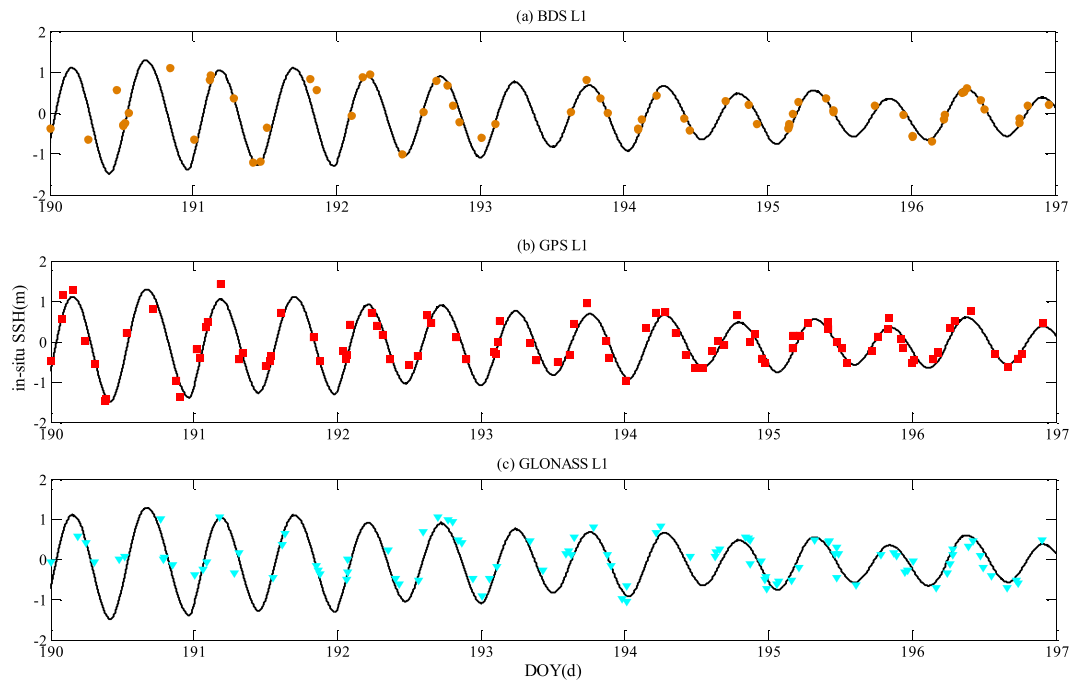


Figure 7. Initial *in-situ* SSH estimation results respectively produced by (a) BDS-R, (b) GPS-R, and (c) GLONASS-R with different frequencies. The black solid line indicates the time series derived from Dzaoudzi tide gauge.

Data Introduction

GPS observations. To verify the feasibility and effectiveness of the proposed GNSS-R based SSH estimation method, the observation data of MAYG station (latitude: -12.78° , longitude: 45.26° , and height: -16.35 m), which is located in Mayotte, France near the Indian Ocean, are used. The TRIMBLE NETR9 receiver and TRM59800.00 antenna is installed in MAYG station, and the data sampling rate is 1 Hz. Because MAYG is one of the Multi-GNSS Experiment (MGEX) stations, so the data of GPS, GLONASS and BDS signals are all recorded. The navigation and observation data can be downloaded from the IGS website (<http://www.igs.org/>). The SNR data of BDS (L1, L5, L7; also called B1, B2, and B3), GPS (L1, L2, L5), and GLONASS (L1, L2) over a period of seven days from DOY 190 to DOY 196 in 2017 were used to evaluate the proposed method. The corresponding elevation angles range between $5^\circ\sim 20^\circ$, whereas the corresponding azimuth angles are between the values $20^\circ\sim 80^\circ$ and $110^\circ\sim 170^\circ$, respectively. The elevation and azimuth angle selection are based on the fact that the multipath signal is strong at low elevation angle. In contrast, the reflected signals from the sea surface are of interest.

Tide gauge observations. The observation data produced by the Dzaoudzi tide gauge, which is about ten meters from the MAYG station, were used as the ground-truth data for evaluating the performance of the proposed SSH estimation method. The sampling rate of the Dzaoudzi tide gauge data is 1 min, which can be downloaded from the Intergovernmental Oceanographic Commission (IOC) website (<http://www.ioc-unesco.org/>).

Results and Discussion

SSH estimation results with Multi-GNSS. Figure 7 shows the *in-situ* SSH estimation results using the L1 signals of GPS, GLONASS, and BDS. The horizontal axis represents the DOY, and the tide gauge observations (black solid line) are also shown for comparison. The GNSS-R based SSH estimates are represented by solid circle, solid square, and solid inverted triangle, respectively for signals of three different satellites.

As can be seen from Fig. 7, there is a significant daily periodicity of *in-situ* SSH changes observed by tide gauge, which is mainly caused by tide and wind variability, as well as sea level pressure variability. There is a good agreement between tide gauge SSH observations and SSH estimates obtained by the GNSS-R methods over a period of seven days. Only a limited number of GNSS satellites can be seen over a certain period of time. Thus, SSH estimations are not uniformly distributed. In some cases, no *in-situ* SSH estimates are available over a quite long time interval. In general, the number of GPS satellites is the largest among the numbers of GPS, BDS, and GLONASS satellites. So, GPS-R has the highest temporal resolution for SSH estimation on average. Figure 8 shows the combined results of SSH estimates with all available GNSS satellites and frequencies. It is interesting to note that the time resolution of SSH is greatly improved.

Table 1 presents the *in-situ* SSH estimation performance in terms of RMSE and correlation coefficients with GPS, BDS, and GLONASS satellite signals of eight different frequency bands. It can be seen from Table 1 that GNSS-R with GPS L1 signal achieves the best performance, i.e., maximum correlation coefficient (0.91) and highest accuracy (RMSE = 0.23 m). Figure 9 shows the histogram of the *in-situ* SSH estimation errors of the three different navigation systems. It can be seen that the errors approximately have a normal distribution. The mean

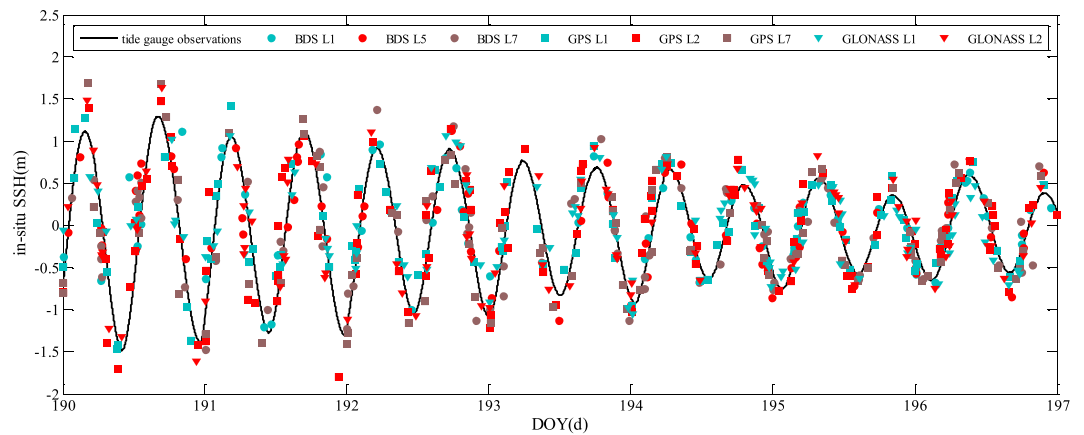


Figure 8. Initial *in-situ* SSH estimation results respectively produced by BDS-R, GPS-R, and GLONASS-R with different frequencies.

Frequency	RMSE/m	Correlation
BDS L1	0.36	0.78
BDS L5	0.32	0.80
BDS L7	0.37	0.77
GPS L1	0.23	0.91
GPS L2	0.34	0.87
GPS L5	0.34	0.88
GLONASS L1	0.31	0.80
GLONASS L2	0.33	0.84
All combined	0.32	0.83

Table 1. The precisions and correlation coefficients of SSH estimation based on BDS-R, GPS-R, and GLONASS-R.

errors are all within 0.02 m, while the standard deviations are 0.31 m, 0.35 m, and 0.32 m for GPS-R, BDS-R, and GLONASS-R, respectively. The means are very close to zero, so the estimation can be considered as unbiased estimation. Figure 10 shows the scatter plot between the tide gauge observations and the GNSS-R SSH estimates. Clearly, the GNSS-R estimates are closely around the tide gauge observations. The RMSEs and correlation coefficients of the combined GNSS-R based estimates are 0.32 m and 0.83, respectively. Although the precision and correlation coefficient are slightly degraded compared with the best results using single frequency band GPS L1, the temporal resolution is increased significantly.

Improved SSH estimates with Wavelet De-noising. As observed from Fig. 8, compared with the tide gauge observations, the GNSS-R based estimates are rather noisy. In order to improve the GNSS-R based *in-situ* SSH estimation precision, we exploit the wavelet de-noising method to reconstruct the tidal waveforms. To produce the best possible wavelet de-noising results, a number of parameters should be selected appropriately^{29,30}. Three of the wavelets i.e. Db6, Haar, and Sym2 are used to reconstruct the tidal waveform. The number of levels for decomposition and reconstruction is set to be 1–8. Table 2 presents the RMSEs and correlation coefficients by using the three different wavelets. It can be seen that when the decomposition level is less than 5, the three different wavelets produce very similar performance. Db6 slightly outperforms the other two wavelets and Db6 with decomposition level of 3 achieves the minimum RMSE. Meanwhile, the decomposition level is greater than 4, the performance of RMSEs and correlation coefficients are degraded, as well as Sym2 with decomposition level of 8 achieves the maximal RMSE. Therefore, only results produced by Db6 wavelet with decomposition level 3 are presented in the following. Figure 11 shows the reconstructed tidal waveforms after wavelet de-noising. For comparison, the tide gauge observations, as well as the initial GNSS-R *in-situ* SSH estimates are also presented. Basically, there is a nice match between the observed and the reconstructed tidal waveforms. The histogram of SSH estimation errors is shown in Fig. 12. By comparing with the results have shown in Fig. 9, the *in-situ* SSH estimation error is significantly reduced and their distribution is more reasonable. The correlation coefficient and RMSE of the wavelet de-noising method are respectively 0.95 and 0.19 m, which are improved by 14.5% and 40.6% over the initial multi-GNSS-R *in-situ* SSH estimation results.

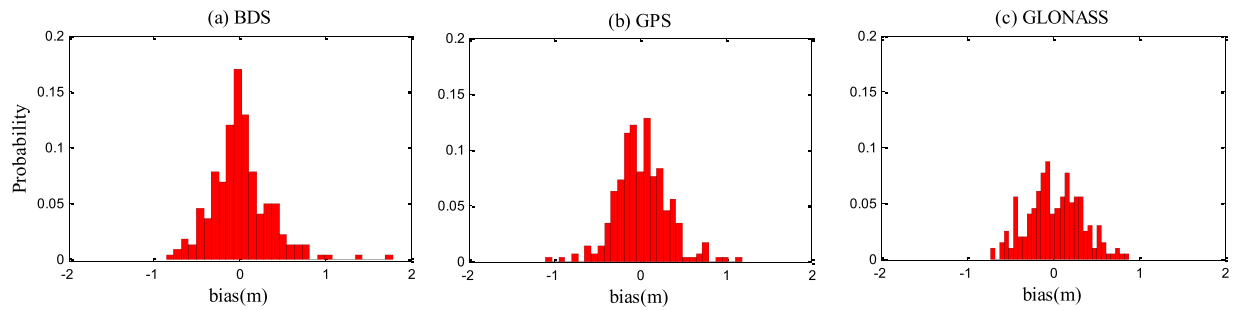


Figure 9. Histogram of the *in-situ* SSH estimation errors of (a) BDS-R, (b) GPS-R, and (c) GLONASS-R.

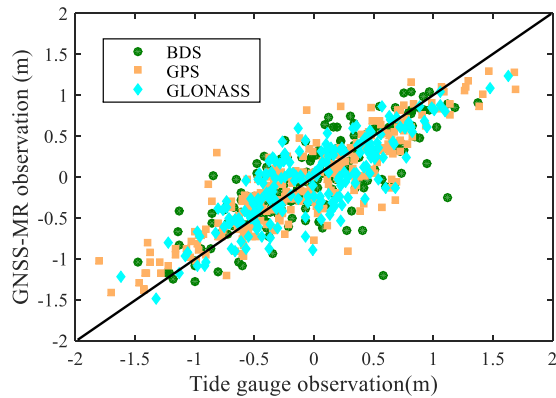


Figure 10. Scatter plot of sea surface height estimates by BDS-R, GPS-R, and GLONASS-R. Tide gauge data are treated as ground-truth. The black line is $X = Y$ line.

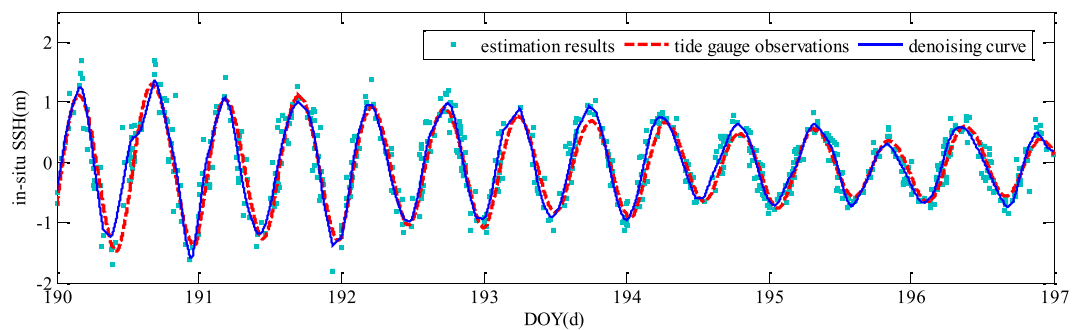


Figure 11. Time series of *in-situ* SSH estimates from initial results and de-noising results.

Level	Db6		Haar		Sym2	
	RMSE (m)	Correlation coefficient	RMSE (m)	Correlation coefficient	RMSE (m)	Correlation coefficient
1	0.21	0.94	0.22	0.94	0.21	0.94
2	0.20	0.95	0.20	0.94	0.19	0.95
3	0.19	0.95	0.22	0.93	0.19	0.95
4	0.19	0.95	0.36	0.83	0.31	0.87
5	0.50	0.70	0.57	0.47	0.55	0.51
6	0.54	0.70	0.60	0.35	0.58	0.45
7	0.54	0.73	0.61	0.39	0.59	0.50
8	0.54	0.72	0.62	0.51	0.59	0.46

Table 2. The precisions and correlation coefficients after wavelet de-noising with different levels.

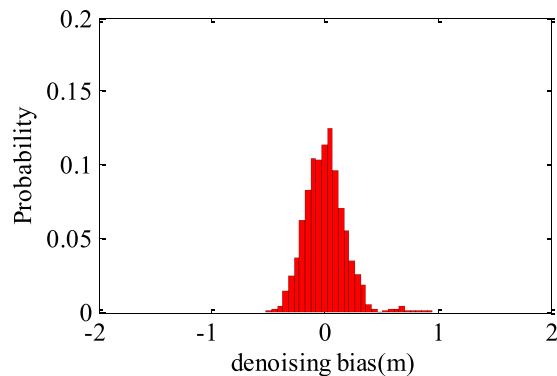


Figure 12. Histogram of SSH estimation errors with the de-noising method.

Conclusions

In this paper, the SNR data of the reflected GNSS satellite signals of different frequency bands, namely BDS (L1, L5, L7), GPS (L1, L2, L5), and GLONASS (L1, L2), were employed to estimate the SSH. The initial *in-situ* SSH estimates were obtained through LSP spectral analysis on the detrended SNR time series. There is a good agreement between tide gauge SSH observations and SSH estimates obtained by the GPS, BDS and GLONASS data. Although the multi-GNSS combined precision and correlation coefficient are slightly degraded compared with GPS L1, the temporal resolution is increased significantly. Wavelet de-noising was applied to the initial *in-situ* SSH estimates to reconstruct the tidal waveform. Compared with tide gauge observations, The research findings demonstrated that the refined *in-situ* SSH estimation based on wavelet de-noising achieved a significant accuracy gain with the RMSE reduced from 0.23 m (GPS L1) and 0.32 m (multiple constellations and multiple frequencies) to 0.19 m, improving the accuracy by 17.4%, 40.6%, respectively. It is worthy of indicating that although these results are inferior to the other research (a few centimeters)³¹, the tidal change at the MAYG station in this paper is up to 3 m, while that of the previous research on other station is within 1 m. Therefore, the relative precision of our method is comparable to the previous research. Furthermore, since water levels and wave dynamics near the coast in storm conditions are very worth researching and discussing^{32,33}, future study will focus on verifying the performance of this proposed method on estimating storm surge water levels.

Received: 19 June 2019; Accepted: 8 October 2019;

Published online: 23 October 2019

References

- Hu, Z. *et al.* Windows of opportunity for salt marsh vegetation establishment on bare tidal flats: The importance of temporal and spatial variability in hydrodynamic forcing. *Journal of Geophysical Research: Biogeosciences* **120**, 1450–1469 (2015).
- Hu, Z. *et al.* Dynamic equilibrium behaviour observed on two contrasting tidal flats from daily monitoring of bed-level changes. *Geomorphology* **311**, 114–126 (2018).
- Mitchum, G. T. Comparison of topex sea surface heights and tide gauge sea levels. *Journal of Geophysical Research Oceans* **99**, 24541–24553 (1994).
- Mitchum, G. T. An improved calibration of satellite altimetric heights using tide gauge sea levels with adjustment for land motion. *Marine Geodesy* **23**, 145–166 (2000).
- Chambers, D. P., Ries, J. C., Shum, C. K. & Tapley, B. D. On the use of tide gauges to determine altimeter drift. *Journal of Geophysical Research Oceans* **103**, 12885–12890 (1998).
- Ablain, M., Cazenave, A., Valladeau, G. & Guinehut, S. A new assessment of the error budget of global mean sea level rate estimated by satellite altimetry over 1993–2008. *Ocean Science* **5**, 193–201 (2009).
- Bouffard, J. *et al.* Introduction and Assessment of Improved Coastal Altimetry Strategies: Case Study Over the Northwestern Mediterranean Sea. *Berlin Heidelberg: Springer*, 297–330 (2011).
- Bindoff, N. L. *et al.* Observations: oceanic climate change and sea level. In: Solomon, S., Qin, D., Manning, M., Chen, Z., Marquis, M., Averyt, K. B., Tignor, M., Miller, H. L. (Eds), *Climate Change 2007: The Physical Science Basis. Contribution of Working Group I to the Fourth Assessment Report of the Intergovernmental Panel on Climate Change*. Cambridge University Press, Cambridge, United Kingdom and New York, NY, USA, 385–433 (2007).
- John, A. C. *et al.* Revisiting the earth's sea-level and energy budgets from 1961 to 2008. *Geophysical Research Letters* **40**, 4066–4066 (2013).
- Yu, K. Tsunami-wave parameter estimation using GNSS-based sea surface height measurement. *IEEE Transactions on Geoscience & Remote Sensing* **53**, 2603–2611 (2015).
- Jin, S., Qian, X. & Kutoglu, H. Snow depth variations estimated from GPS-reflectometry: a case study in alaska from l2p SNR data. *Remote Sensing* **8**, 63 (2016).
- Nievinski, F. G. & Larson, K. M. Inverse modeling of GPS multipath for snow depth estimation—Part II: application and validation. *IEEE Transactions on Geoscience & Remote Sensing* **52**, 6564–6573 (2014).
- Larson, K. M. *et al.* Use of GPS receivers as a soil moisture network for water cycle studies. *Geophysical Research Letters* **35**, 851–854 (2010).
- Löfgren, J. S., Haas, R. & Scherneck, H. G. Sea level time series and ocean tide analysis from multipath signals at five GPS sites in different parts of the world. *Journal of Geodynamics* **80**, 66–80 (2014).
- Katzberg, S. J., Torres, O., Grant, M. S. & Masters, D. Utilizing calibrated GPS reflected signals to estimate soil reflectivity and dielectric constant: Results from SMEX02. *Remote Sensing of Environment* **100**, 17–28 (2006).
- Treuhaft, R. N., Lowe, S. T., Zuffada, C. & Chao, Y. 2-cm GPS altimetry over crater lake. *Geophysical Research Letters* **28**, 4343–4346 (2001).

17. Roussel, N. *et al.* Sea level monitoring and sea state estimate using a single geodetic receiver. *Remote Sensing of Environment* **171**, 261–277 (2015).
18. Foti, G. *et al.* Spaceborne GNSS-Reflectometry for ocean winds: First results from the UK TechDemoSat-1 mission: Spaceborne GNSS-R: First TDS-1 results. *Geophysical Research Letters* **42**, 5435–5441 (2015).
19. Rius, A., Cardellach, E. & Martin-Neira, M. Altimetric analysis of the sea-surface GPS-reflected signals. *IEEE Transactions on Geoscience & Remote Sensing* **48**, 2119–2127 (2010).
20. Carreno-Luengo, H., Park, H., Camps, A., Fabra, F. & Rius, A. GNSS-R derived centimetric sea topography: an airborne experiment demonstration. *IEEE Journal of Selected Topics in Applied Earth Observations & Remote Sensing* **6**, 1468–1478 (2013).
21. Anderson, K. D. A. GPS tide gauge. *GPS World Showcase* **6**, 44–44 (1995).
22. Larson, K. M., Löfgren, J. S. & Haas, R. Coastal sea level measurements using a single geodetic GPS receiver. *Advances in Space Research* **51**, 1301–1310 (2013).
23. Santamaria-Gómez, A., Watson, C., Gravelle, M., King, M. & Wöppelmann, G. Levelling co-located GNSS and tide gauge stations using GNSS reflectometry. *Journal of Geodesy* **89**, 241–258 (2015).
24. Jin, S., Qian, X. & Wu, X. Sea level change from BeiDou Navigation Satellite System-Reflectometry (BDS-R): First results and evaluation. *Global & Planetary Change* **149**, 20–25 (2017).
25. Vanderplas, J. T. *Understanding the lomb-scargle periodogram*. (2017).
26. Grossmann, A. & Morlet, J. Decomposition of hardy functions into squareintegrable wavelets of constant shape. *Siam Journal on Mathematical Analysis* **15**, 723–736 (1984).
27. Peng, Z. K. & Chu, F. L. Application of the wavelet transform in machine condition monitoring and fault diagnostics: a review with bibliography. *Mechanical Systems & Signal Processing* **18**, 199–221 (2004).
28. Mallat, S. G. A Theory for Multiresolution Signal Decomposition: The Wavelet Representation. *IEEE Pattern Anal Mach Intell* **11**, 674–693 (1989).
29. Chui, C. K. An introduction to wavelets, wavelet analysis and its application. *Acta Médica Costarricense* **53**, 37–41 (1992).
30. Torrence, C. & Compo, G. P. A practical guide to wavelet analysis. *Bull Am Meteorol Soc* **79**, 61–78 (1998).
31. Strandberg, J., Hobiger, T. & Haas R. Inverse modelling of GNSS multipath for sea level measurements - initial results. *2016 IEEE International Geoscience and Remote Sensing Symposium (IGARSS)*, Beijing, 1867–1869 (2016).
32. Hu, Z., Suzuki, T., Zitman, T., Uijtewaal, W. & Stive, M. Laboratory study on wave dissipation by vegetation in combined current-wave flow. *Coastal Engineering* **88**, 131–142 (2014).
33. Suzuki, T. *et al.* Non-hydrostatic modeling of drag, inertia and porous effects in wave propagation over dense vegetation fields. *Coastal Engineering* **149**, 49–64 (2019).

Acknowledgements

This study was supported by the Funds for Creative Research Groups of China (Grant No. 41721003) and the National Key Research Development Program of China (No. 2016YFB0501803, No. 2017YFB0503402). We thank the International GNSS Service Organization (IGS) for providing GNSS observations and the Intergovernmental Oceanographic Commission for tide gauge observations. Meanwhile, we would also like to express our gratitude to Prof. Kegen Yu and Mr. Mohamed Freeshah for their help of language editing.

Author contributions

Fei Guo and Fade Chen conceived and designed the experiments; Fade Chen and Lilong Liu performed the experiment and analyzed the experimental data; All authors were involved in the writing of this paper.

Competing interests

The authors declare no competing interests.

Additional information

Correspondence and requests for materials should be addressed to F.G.

Reprints and permissions information is available at www.nature.com/reprints.

Publisher's note Springer Nature remains neutral with regard to jurisdictional claims in published maps and institutional affiliations.



Open Access This article is licensed under a Creative Commons Attribution 4.0 International License, which permits use, sharing, adaptation, distribution and reproduction in any medium or format, as long as you give appropriate credit to the original author(s) and the source, provide a link to the Creative Commons license, and indicate if changes were made. The images or other third party material in this article are included in the article's Creative Commons license, unless indicated otherwise in a credit line to the material. If material is not included in the article's Creative Commons license and your intended use is not permitted by statutory regulation or exceeds the permitted use, you will need to obtain permission directly from the copyright holder. To view a copy of this license, visit <http://creativecommons.org/licenses/by/4.0/>.

© The Author(s) 2019